Arbon (TG) - Evangelische Kirche (SARE)
SITE CHARACTERIZATION REPORT

Jan BURJÁNEK, Manuel HOBIGER, Donat FÄH

Sonneggstrasse 5 CH-8092 Zürich Switzerland; E-mail: `burjanek@sed.ethz.ch`

Last modified : May 7, 2020

Abstract

Ambient vibration array measurements were performed to characterize the site of the strong-motion station SARE, located in Arbon (TG). The site is located on alluvia near Lake Constance. The new station was installed in the framework of the Renewal of the Swiss strong motion network. In order to characterize the velocity profile under the station, array measurements with a $260\,\mathrm{m}$ aperture were performed. The measurements were successful and allowed deriving a velocity model for this site.

We found a first layer of approximately $12\,\mathrm{m}$ characterized by a linear increase of shear wave velocities from $200\,\mathrm{m/s}$ to $500\,\mathrm{m/s}$, corresponding likely to unconsolidated soils or moraine. Below, the velocity is increasing less rapidly from $500\,\mathrm{m/s}$ to $800\,\mathrm{m/s}$ down to $200\,\mathrm{m}$. The bedrock depth is not very well resolved, a strong jump of shear wave velocities is not required even by the singularity of the ellipticity angle. Nevertheless, shear wave velocity increases significantly below $200\,\mathrm{m}$. This corresponds likely to the base of the unconsolidated sediments which is at $170\,\mathrm{m}$ according to Swisstopo.
$V_{s,30}$ is around $374\,\mathrm{m/s}$ and corresponds to ground type B in Eurocode 8 [CEN, 2004], and C for SIA261 [SIA, 2014].

The theoretical 1D SH transfer function and impedance contrast of the quarter-wavelength velocity computed from the inverted profiles show moderate amplifications and are compared with the empirical amplification function.

Contents

1   Introduction

The station SARE (Arbon - Evangelische Kirche) is part of the the Swiss Strong Motion Network (SSMNet). SARE has been installed in the framework of the SSMNet renewal project on December 19, 2014. This project includes also the site characterization. Passive array measurements have been selected as a standard tool to investigate these sites. An array measurement was carried out on June 26, 2016 in the garden, grassland and streets close to the Protestant church (Fig. 1). The array consisted of five eccentric rings (polygons). One of the vertices of the smallest ring was close to SARE, whereas SARE is located rather at the center of the outer rings. Such an irregular configuration was selected due to limited free areas. This report presents the measurement setup, the results of the H/V analysis and of the array processing of the surface waves (dispersion and ellipticity curves). Then, an inversion of these results into velocity profiles is performed. Standard parameters are derived to evaluate the amplification at this site.

Figure 1: Picture of the site.

2 Geology

The surface geological map indicates that the site is located on moraine (Fig. 2). However, the subsurface structure is more complex. The gravimetric atlas of Switzerland (Federal Office of Topography swisstopo) shows at the site large-scale anomaly elongated in the east-west direction. Moreover, the model of the bedrock surface (or Quaternary base) produced by Swisstopo shows a relatively deep valley (down to 250 m at Arbon), which follows the gravimetric anomaly and is filled with Quaternary sediments (Fig. 3). This sedimentary body is quite narrow (up to 2 km at Arbon) and extends further west/northwest to cities of Weinfelden and Frauenfeld (tenths of km away), but is hardly recognizable from the surface topography (especially near Arbon). These sediments are likely of alluvial origin and were probably deposited during prehistoric formation of Lake Constance. The bedrock consists of marine and fluvial deposits of Oligocene and Miocene age (Molasse). The station SARE is therefore located close to the edge of a deep basin where resonance from the Quaternary sediments is expected.
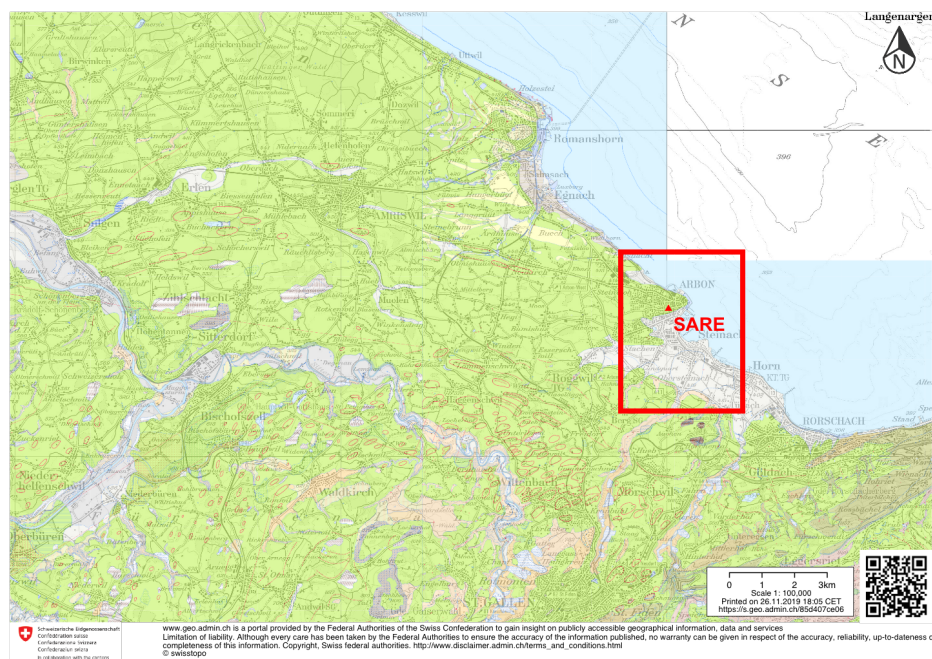

Figure 2: Surface geological map of the area of station SARE (red triangle). The red rectangle indicates the area of Arbon. The white color refers to alluvia and the green area to moraines.
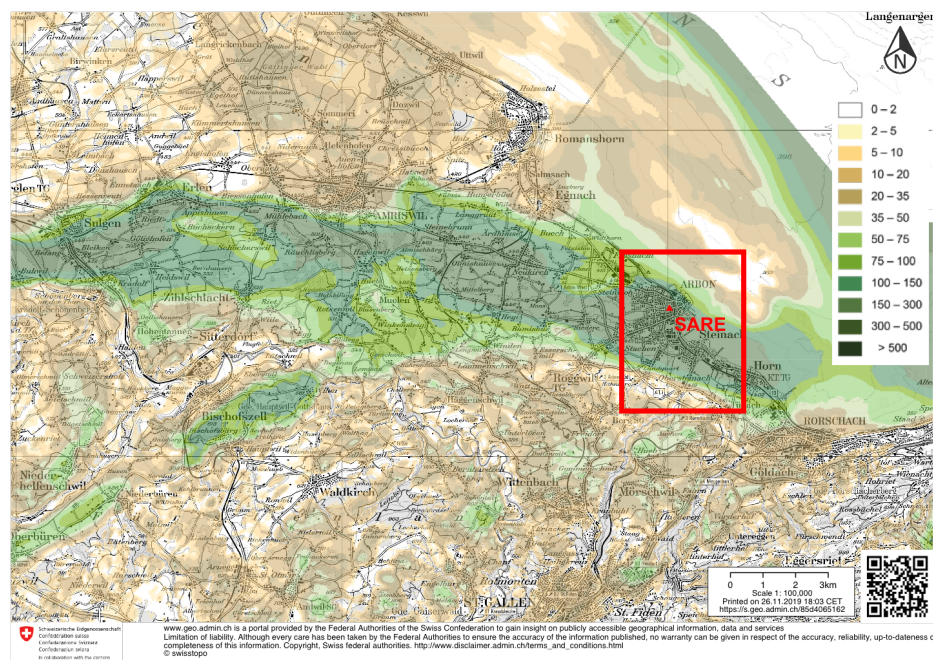
Figure 3: Thickness of unconsolidated sediments in the area of station SARE (red triangle). The red rectangle indicates the area of Arbon. The colorscale shows the thickness of unconsolidated sediments in meters.

3 Experiment description

3.1 Ambient Vibrations

The ground surface is permanently subjected to ambient vibrations due to:

- natural sources (ocean and large-scale atmospheric phenomena) below $1\,\mathrm{Hz}$,

- local meteorological conditions (wind and rain) at frequencies around $1\,\mathrm{Hz}$,

- human activities (industrial machines, traffic...) at frequencies above $1\,\mathrm{Hz}$ [Bonnefoy-Claudet et al., 2006].

The objective of the measurements is to record these ambient vibrations and to use their propagation properties to infer the underground structure. First, the polarization of the recorded waves (H/V ratio) is used to derive the resonance frequencies of the soil column. Second, the arrival time delays at many different stations are used to derive the velocity of surface waves at different frequencies (dispersion). The information (H/V, dispersion curves) is then used to derive the properties of the soil column using an inversion process.

3.2 Equipment

For these measurements 12 Centaur dataloggers named NR42-NR49, NR52-55 and 16 Lennartz 3C 5 s seismometers were available (see Tab. 1). Each datalogger can record on 2 ports: A (channels EH1, EH2, EH3 for Z, N, E directions) and B (channels EH4, EH5, EH6 for Z, N, E directions). Time synchronization was ensured by GPS. The sensors were placed on a metal tripod, in a $20\,\mathrm{cm}$ deep hole, when necessary, for better coupling with the ground.

Digitizer	Model	Number	Resolution
	Centaur	12	$24\,\mathrm{bits}$
Sensor type	**Model**	**Number**	**Cut-off frequency**
Velocimeter	Lennartz 3C	16	$0.2\,\mathrm{Hz}$

Table 1: Equipment used.

3.3 Geometry of the arrays

Two array configurations were used. In the first configuration, 4 eccentric irregular rings of approximately 5, 10, 25 and $75\,\mathrm{m}$ radius were deployed for a total of 16 sensors. Station SARE was located next to the smallest ring. The configuration is quite irregular because of many obstacles (trees, buildings, fences). The second configuration includes two eccentric outer rings of 40 and $130\,\mathrm{m}$, respectively (plus few stations in the vicinity), 14 sensors in total. The second configuration is very irregular, as we were not allowed to place sensors in the middle of the grassland in the afternoon. The minimum inter-station distance and the aperture are therefore 5 / $150\,\mathrm{m}$ and 25 / $260\,\mathrm{m}$, respectively. The experimental setup is displayed in Fig. 4. The final usable datasets are detailed in section 4.2.
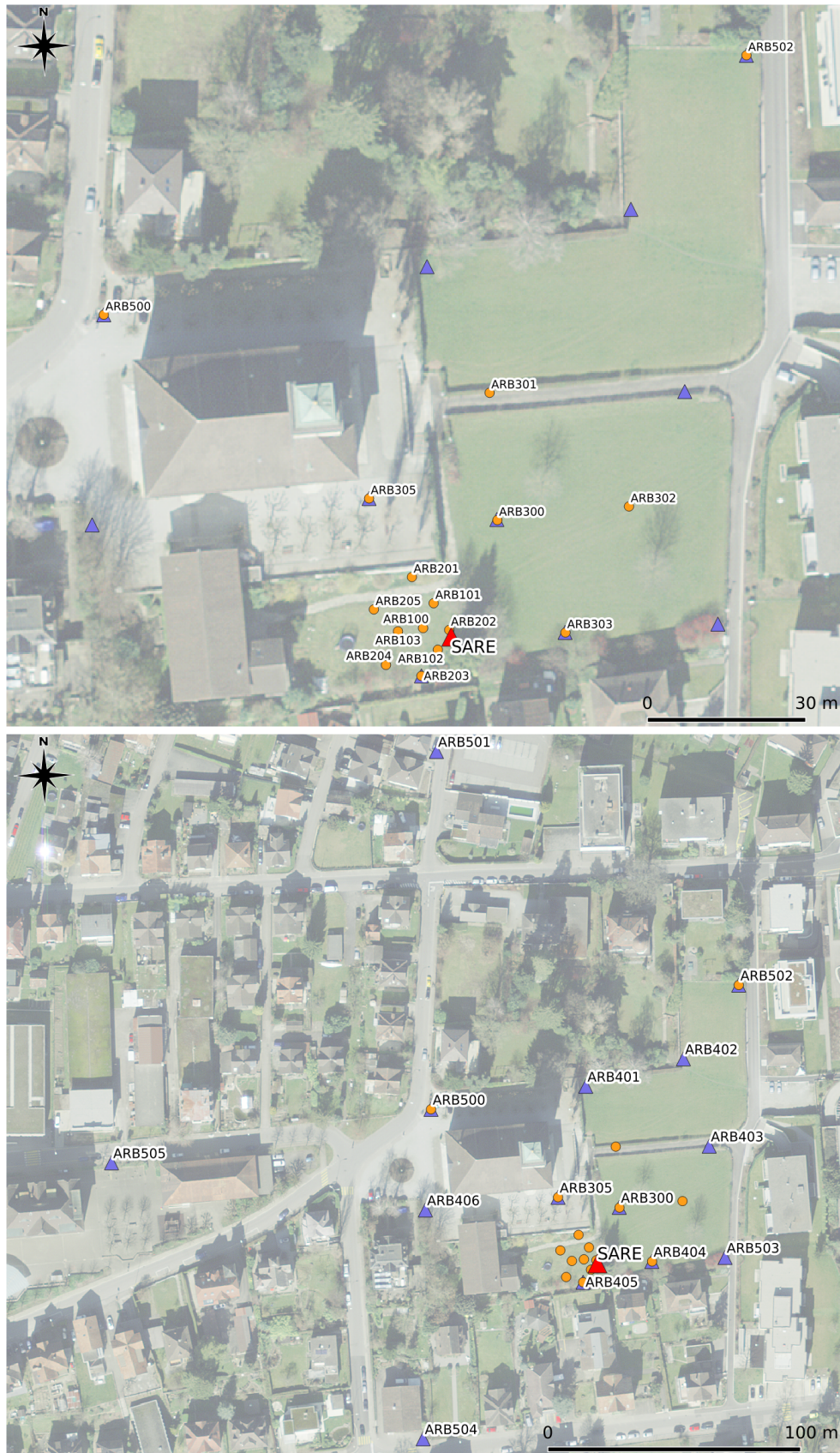
Figure 4: Geometry of the arrays. Orange circles refer to the first configuration, purple triangles refer to the second configuration, and red triangle to station SARE.

3.4 Positioning of the stations

The sensor coordinates were measured using a differential GPS device (Leica Viva GS10), including one rover station and using the Real Time Kinematic technique provided by Swisstopo. It allows an absolute positioning with an accuracy better than $6\,\mathrm{cm}$ on the Swissgrid. This accuracy was reached for all stations.

4   Data quality

4.1   Usable data

The largest time windows were extracted for which all the sensors of the array were correctly placed and the GPS synchronization was ensured. The recordings are generally consistent. Incoherent high amplitude signals are mainly due to the differential GPS measurement. The characteristics of the datasets are detailed in Tab. 2.

4.2   Data processing

The data were first converted to SAC format including in the header the coordinates of the point (CH1903 system), the recording component and a name related to the position. The name is made of 3 letters characterizing the location (ARB here), 1 digit for the ring and 2 more digits for the number in the ring (zero for the central station of the corresponding ring - if present). The recordings were not corrected for the instrumental response.

Dataset	Date	Start time (UTC)	Length	F_s	Min. inter-distance	Aperture	# of points
1	2016/06/29	08:20	120 min	200 Hz	10 m	150 m	16
2	2016/06/29	13:00	110 min	200 Hz	25 m	260 m	14

Table 2: Usable datasets.

5 H/V processing

5.1 Processing method and parameters

In order to process the H/V spectral ratios, several codes and methods were used. The multitaper method of the spectra estimates [Prieto et al., 2009] was applied as well with the time bandwidth product of 2.5 and 4 tapers. The classical method of Fäh et al. [2001] was also performed.

Moreover, the time-frequency analysis method [Fäh et al., 2009] was used to estimate the ellipticity function more accurately using the Matlab code of V. Poggi. In this method, the time-frequency analysis using the Wavelet transform is computed for each component. For each frequency, the maxima over time (10 per minute with at least $0.1\,\text{s}$ between each) in the TFA are determined. The Horizontal to Vertical ratio of amplitudes for each maximum is then computed and statistical properties for each frequency are derived. A Cosine wavelet with parameter 9 is used. The mean of the distribution for each frequency is stored. For the sake of comparison, the time-frequency analysis of Fäh et al. [2001], based on the spectrogram, was also used.

The ellipticity extraction using the wavefield decomposition method [Maranò et al., 2012] (see section on array analysis) was also performed.

Method	Freq. band	Win. length	Anti-trig.	Overlap	Smoothing
Standard H/V Multitaper	$0.2 - 40\,\text{Hz}$	$200\,\text{s}$	No	-	-
Standard H/V D. Fäh	$0.2 - 20\,\text{Hz}$	$30\,\text{s}$	No	75%	-
H/V TFA D. Fäh	$0.2 - 20\,\text{Hz}$	Specgram	No	-	-
H/V TFA V. Poggi	$0.2 - 20\,\text{Hz}$	Cosine wpar=9	No	-	No

Table 3: Methods and parameters used for the H/V processing.

5.2 Results

All the methods to compute H/V ratios are compared at the array centre on Fig. 5, in which the classical methods were divided by $\sqrt{2}$ to correct for the Love wave contribution [Fäh et al., 2001]. Overall, the classical and TFA methods match well. Too strong smoothing can result in smearing of the fundamental peak.

All points of the array show a similar shape in their H/V with a pronounced peak (Fig. 6) at $0.8\,\text{Hz}$. The H/V curves for stations of the second configuration are shown in Fig. 6 together with the ellipticity curves for two modes obtained by the Wavedec technique Maranò et al. [2012]. The fundamental peaks and right flanks of the ellipticity curves show good agreement between the different stations and the ellipticity of the fundamental mode obtained with the array method for 4 - 7 Hz, except for station ARB505, which is an outlier. In conclusion, the fundamental peak at the site is at $0.8\,\text{Hz}$, with a peak H/V amplitude around 6 for the TFA methods.
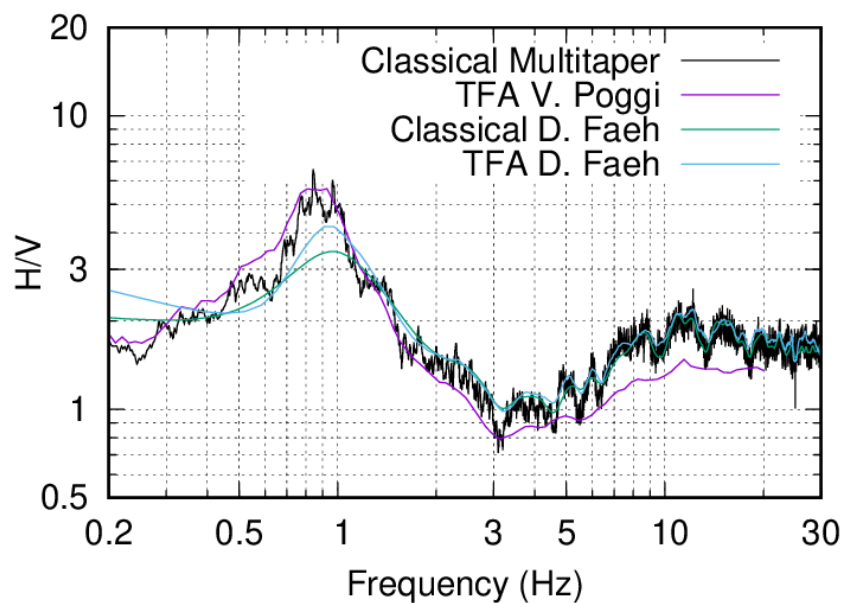
Figure 5: H/V spectral ratios for point ARB100 using the different codes. Classical methods were divided by $\sqrt{2}$.
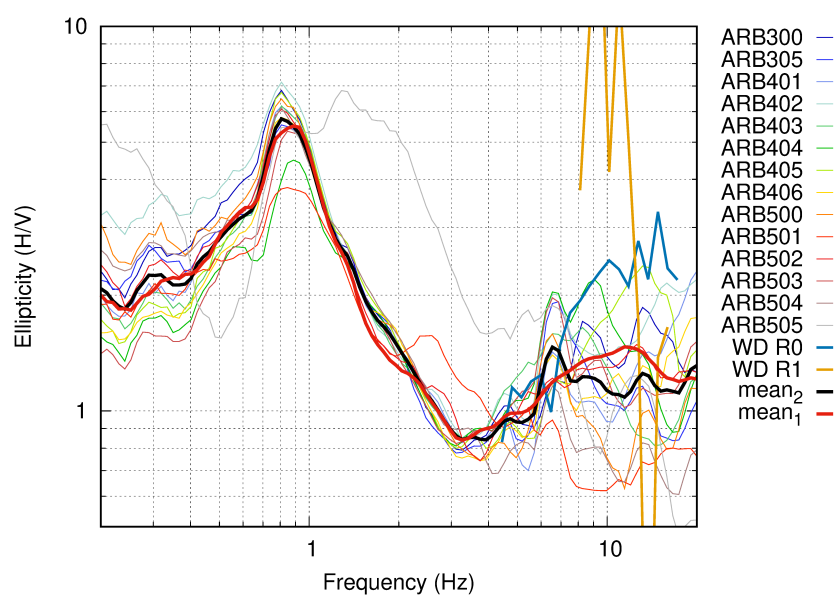

Figure 6: H/V spectral ratios (time-frequency analysis code V. Poggi) for the second array configuration (thin colored curves), ellipticity curves obtained by the array Wavedec technique (thick orange and blue curves), mean TFA H/V curves for the first (thick red) and second (thick black) array configurations.

5.3   Polarization analysis

The polarization analysis on the array data was performed using the method of Burjánek et al. [2010]. Most of the points (Fig. 7) show a particular consistent (but weak) polarization in the frequency band $0.7 - 3\,\text{Hz}$. The origin of this directionality is not clear, but the edge of the sedimentary basin might play a role.
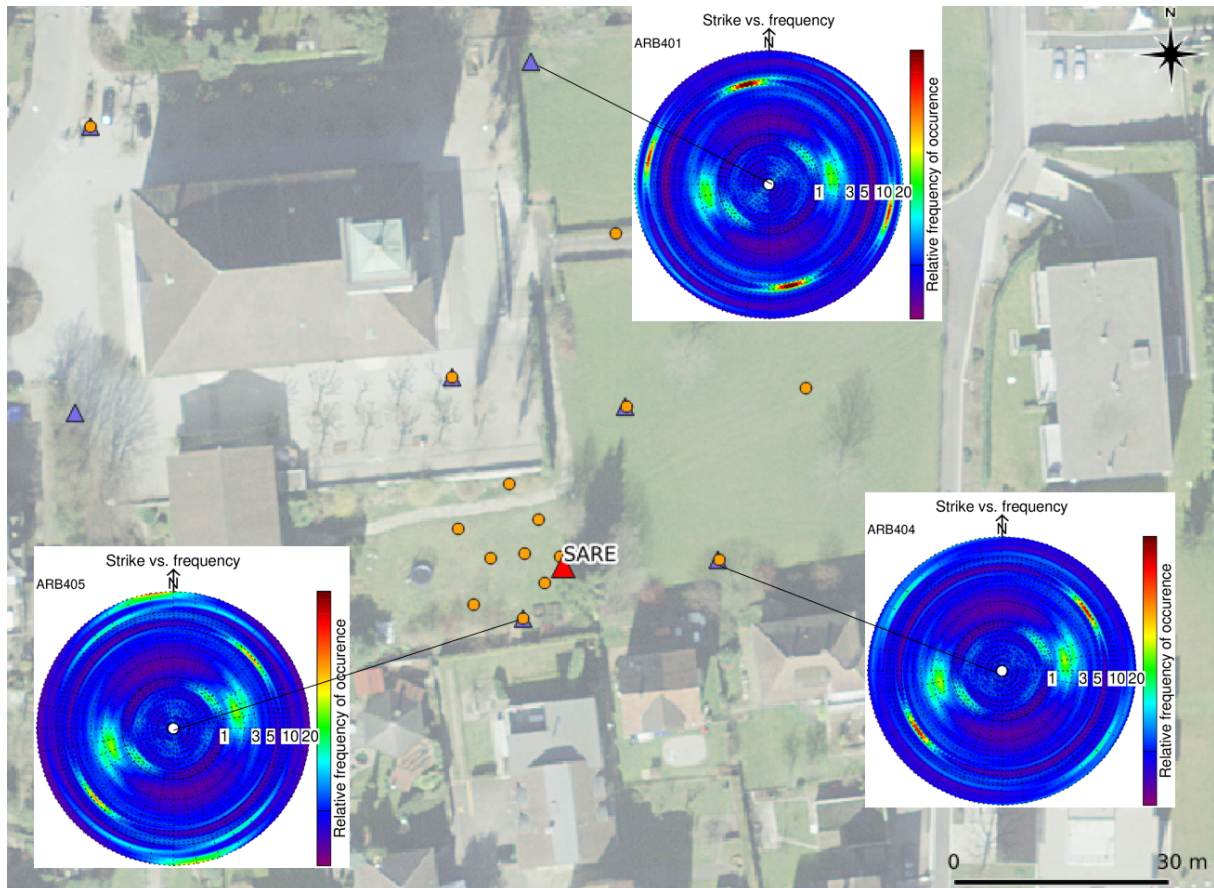

Figure 7: Strike of the polarization for three selected stations.

6   Array processing

6.1   Processing methods and parameters

A 3C array analysis [Fäh et al., 2008] was performed using both the array_tool_3C software [Poggi and Fäh, 2010] (HRFK) and Geopsy http://www.geopsy.org software (FK). It allows us to derive Rayleigh and Love wave modes including the Rayleigh wave ellipticity. Finally, 3C Wavedec technique was applied as well [Maranò et al., 2012] in order to estimate both dispersion and ellipticity curves.

6.2   Obtained dispersion curves

The analysis of the transverse component was quite straightforward (Fig. 8). Wavedec provided reasonable histograms in the FK space for the first array configuration in a broad frequency range (5 - 19 Hz). However, the picked dispersion curve was significantly biased towards higher velocities for frequencies below 8 Hz with respect to the 3C HRFK analysis for the first configuration and even more biased with respect to results for the second (larger) array configuration. This a problem of the resolution limit, since the picked dispersion curve hits the lower resolution limit of classical beamforming as defined in Wathelet et al. [2008]. There were only three stations in the outermost ring in the first configuration and the radial component of the Rayleigh wave fundamental mode is likely smeared into the transverse component (compare their velocities). In contrast, Wavedec outperformed 3C HRFK in the frequency range 10 - 19 Hz. All Wavedec, 3C HRFK and 3C FK curves provide reasonable and consistent results for the second array configuration in the frequency range of 1.5 - 8 Hz for the fundamental mode. Moreover, a higher mode could be picked as well in the frequency range of 4 - 6 Hz

The analysis of the vertical and radial components was more complicated (Fig. 9), two Rayleigh wave modes were very close to each other in the frequency range of 2 - 4 Hz. A jump of the energy between the two modes is well visible on the FK analysis of the vertical component of the second array configuration. The Wavedec analysis of the first array configuration shows two modes, the fundamental one in the frequency range of 4 - 17 Hz and the higher one in the frequency range of 8 - 16 Hz. The HRFK analysis (vertical component) for the first configuration detects only the higher mode for frequencies above 7 Hz (velocities in agreement with Wavedec), while FK detects the fundamental mode up to 10 Hz (velocities in agreement with Wavedec). The Wavedec analysis of the second array configuration shows only the fundamental mode in the frequency range of 4 - 8 Hz. HRFK of the second array configuration shows both modes, the fundamental one in the frequency range of 1.5 - 7 Hz, and the weaker higher in the frequency range of 4 - 10 Hz. The two modes become very close below 4 Hz, an osculation point is likely present at 2 Hz.

All picked curves, trimmed according to the resolution limits, are presented together on Fig. 10.
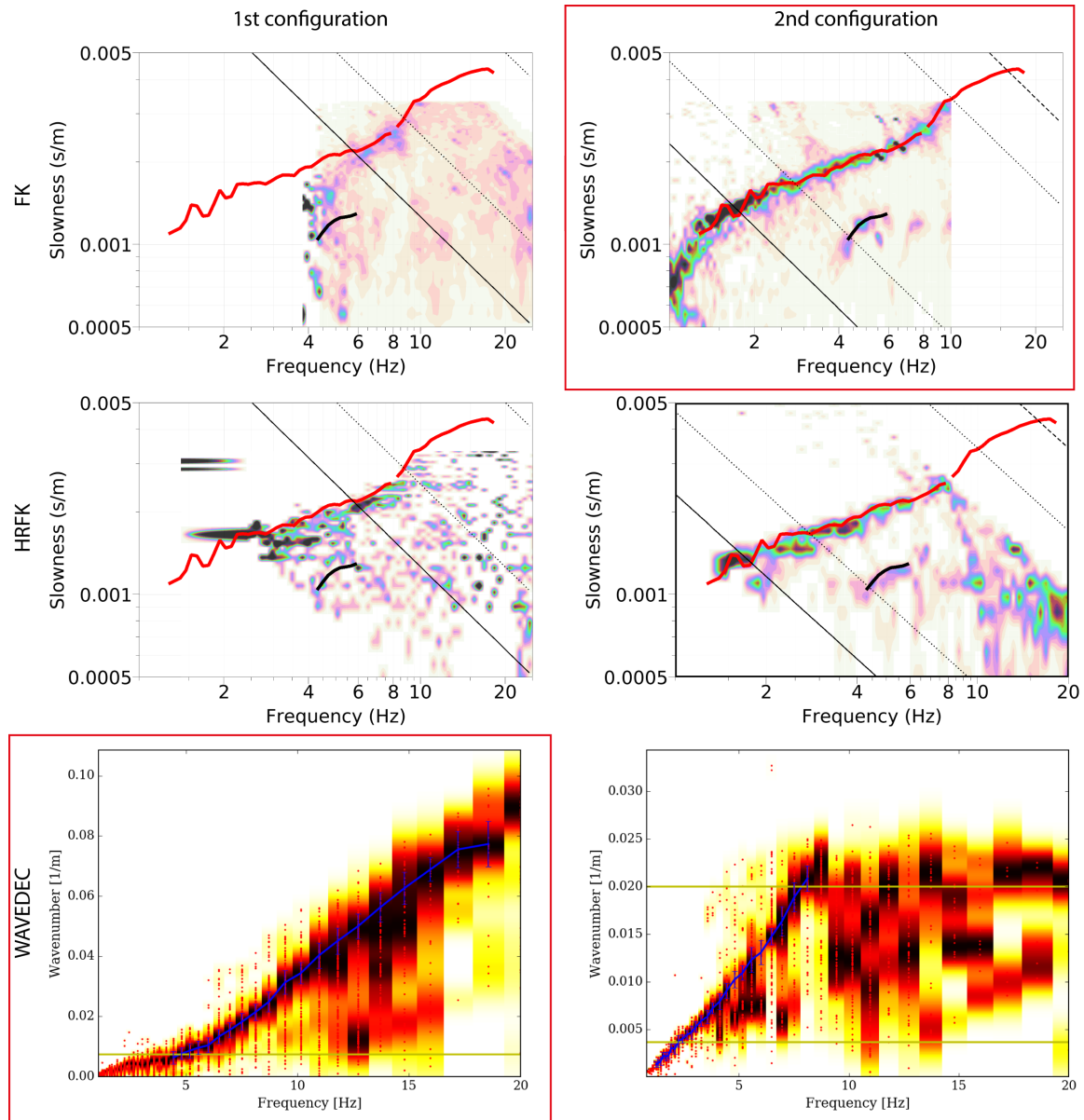
Figure 8: Array analysis of the transverse component and final pick of the Love wave dispersion curves. The results in the red frames were used for the final picking of the dispersion curve chunks. That is, the high frequency chunk of the Love wave fundamental mode (in red in the first two lines) is picked from the Wavedec results, while the low-frequency chunk of the Love wave fundamental (in red) and first higher mode (in black) from the results of classical 3C FK analysis. This final pick is present on all plots for FK and HRFK just to check for consistency. The results of Wavedec indicate only the pick of the fundamental mode (in blue).
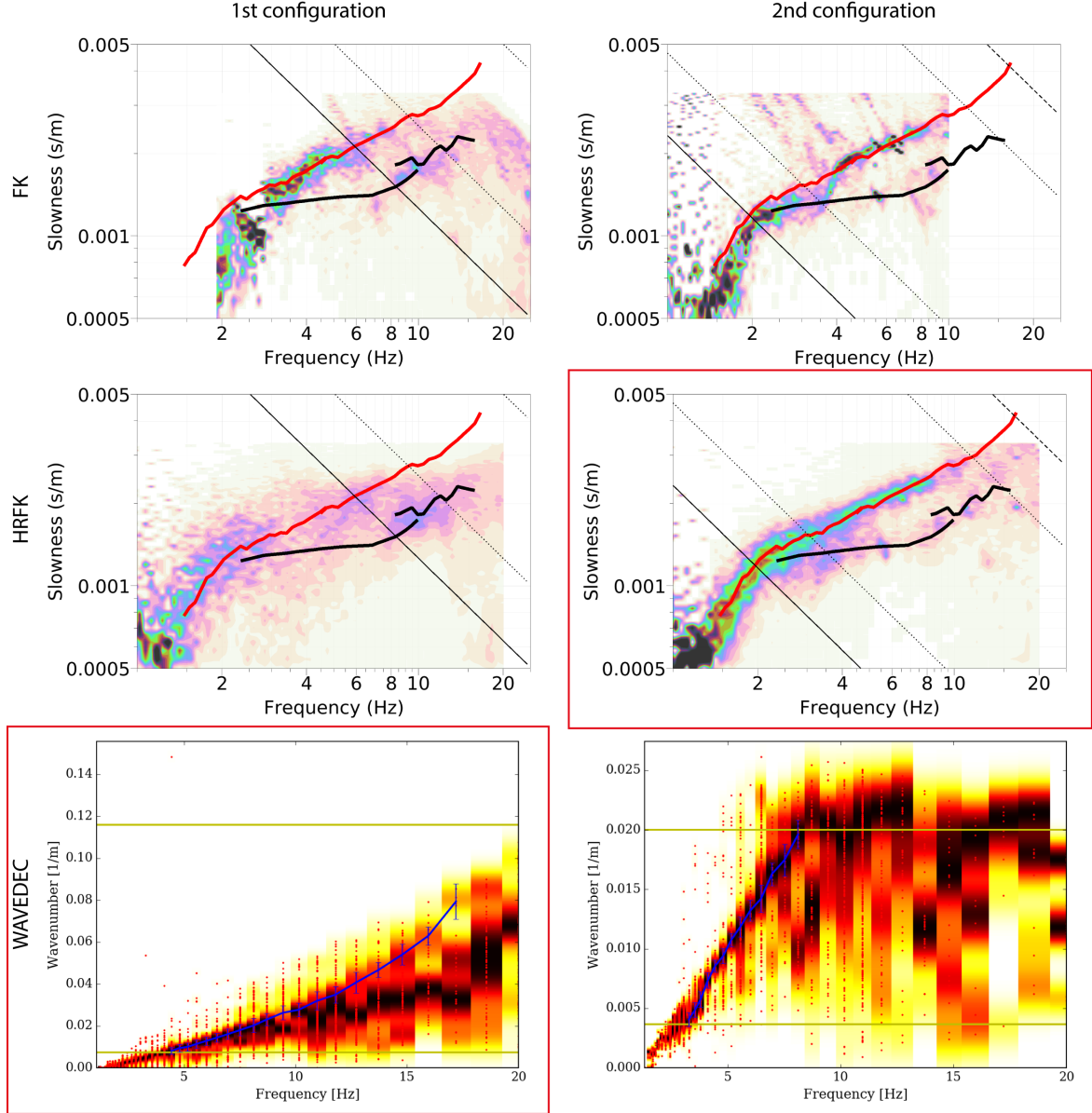
Figure 9: Array analysis of the vertical component and final pick of the Rayleigh wave dispersion curves. The results in the red frame were used for the final picking of the dispersion curve chunks. That is, the high frequency chunk of the Rayleigh wave fundamental mode (in red in the two first lines) and first higher mode (in black) are picked from the Wavedec results, while the low-frequency chunk of the Rayleigh wave fundamental and first higher Rayleigh mode from the results of high-resolution 3C FK analysis. This final pick is present on all plots for FK and HRFK just to check for consistency. The results of Wavedec indicate only the pick of the fundamental mode (in blue).
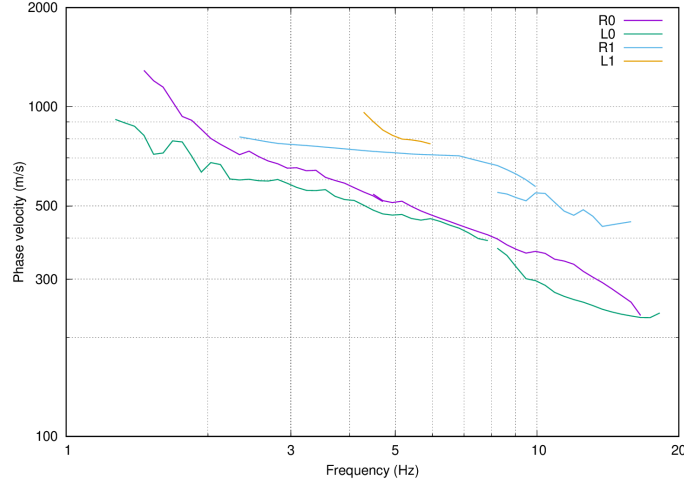
Figure 10: Picked dispersion curves.

6.3   Obtained ellipticity angle

The ellipticity angles of the fundamental and the first higher Rayleigh wave modes were estimated by Wavedec (Fig. 11). It was possible to pick the ellipticity of the higher mode (8 - $16\,\text{Hz}$) from the first array configuration, which shows two singularities. The ellipticity of the fundamental mode (5 - $19\,\text{Hz}$) obtained from the first array configuration shows purely retrograde motion, while the ellipticity of the fundamental mode (below $8\,\text{Hz}$) obtained from the second array configuration crosses zero approximately at $3\,\text{Hz}$, although it was not possible to exactly pick the dispersion curve below $4\,\text{Hz}$. This frequency corresponds well with the trough in the ellipticity curves at 3 Hz shown in HV000. Therefore a singularity (retrograde - prograde transition) should be present at the fundamental frequency (below $0.8\,\text{Hz}$).
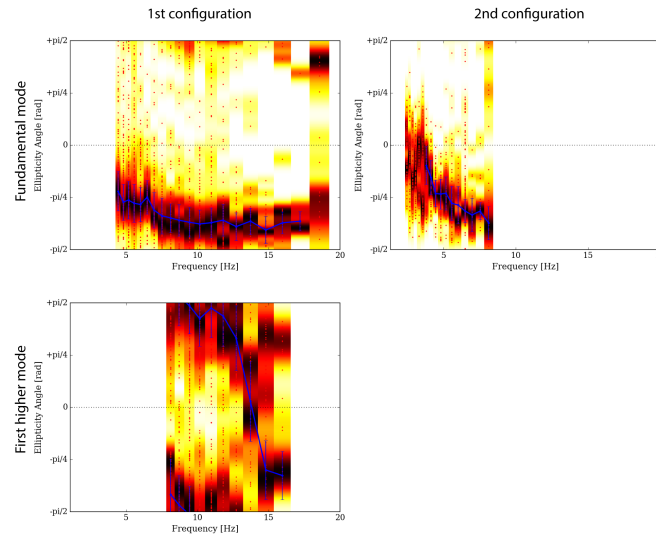

Figure 11: Picked ellipticity angle curves from Wavedec.

7   Inversion and interpretation

7.1   Inversion

For the inversion, the fundamental and first higher mode dispersion curves of both Love and Rayleigh waves between 1.5 and $19\,\mathrm{Hz}$, as well as the ellipticity of the fundamental and higher mode were used as simultaneous targets without standard deviation to avoid different weighting. The new version of Dinver inverts directly the ellipticity angle. The incomplete ellipticity angle curve for the fundamental mode retrieved by Wavedec was therefore extrapolated by $arctan(H/V)$ with the sign retrieved from Wavedec (negative below fundamental frequency of $0.8\,\mathrm{Hz}$, positive between 0.8 and $3\,\mathrm{Hz}$, and again negative above $3\,\mathrm{Hz}$), see Fig. 12. Several inversions were run with the older version of Dinver, capable to invert ellipticity, to verify this approach. A weight of 0.1 was assigned to the ellipticity angle curve. All curves were resampled using 100 points between 0.2 and $20\,\mathrm{Hz}$ in log scale.
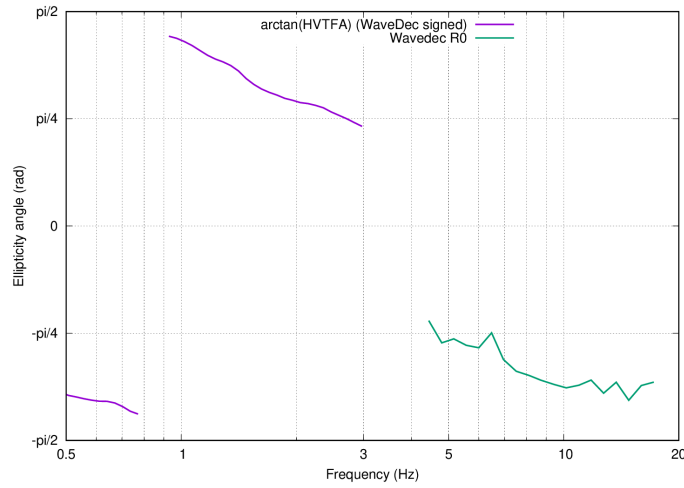

Figure 12: Ellipticity target used in the inversion.

The inversion was performed using the Improved Neighborhood Algorithm (NA) Wathelet [2008] implemented in the Dinver software.

The velocity was assumed to increase with depth. The Poisson ratio was allowed to have values in the range 0.2-0.45 in each layer. The density was fixed to $2300\,\mathrm{kg/m^3}$. A number of inversions with fixed layer depths were performed (testing different parametrizations). Fine layering close to the surface was introduced, to capture the shallow strong interface. The resulting parametrization, which is considered in this report, consisted of 22 layers on top of a half-space. In total, 110000 models were generated during the inversion (NA parameters: $Ns0 = 100000$, $Ns = 10000$, $Nr = 50$) with this parametrization and results are shown in Fig. 13. Moreover, an additional parametrization with a free-depth bedrock was assumed, to represent the potential strong velocity jump related to the deep base of the unconsolidated sediments. This parametrization was created from the one described above (22 layers) by removing 10 bottom layers. Therefore it consisted of 12 layers on top of a half-space. In total, 110000 models were generated during the inversion (NA parameters: $Ns0 = 100000$, $Ns = 10000$, $Nr = 50$) with this parametrization and results are shown in Fig. 14. Both parametrizations allow for a very

good reproduction of the observed dispersion curves and the ellipticity curve of the fundamental mode (Fig. 13, Fig. 14).

We found a first layer of approximately $12\,\mathrm{m}$ characterized by linear increase of shear wave velocities from $200\,\mathrm{m/s}$ to $500\,\mathrm{m/s}$ corresponding likely to unconsolidated soils or moraine. Below, the velocity is increasing less rapidly from $500\,\mathrm{m/s}$ to $800\,\mathrm{m/s}$ down to $200\,\mathrm{m}$. The bedrock depth is not very well resolved, a strong jump of shear wave velocities is not required even by the singularity of the ellipticity angle. Nevertheless, shear wave velocity increases significantly below $200\,\mathrm{m}$. This corresponds likely to the base of the unconsolidated sediments which is at $170\,\mathrm{m}$ according to Swisstopo.

The dispersion curves are well represented, and the ellipticity curve is satisfactorily reproduced as well, except the ellipticity of the higher mode, which was not possible to fit together with the other data (trial inversions, not shown here). The representative set of models for further elaboration is shown in Fig. 15. This set consists of the best-fitting models and 20 additional models for both parametrizations (42 models in total). These models were randomly selected in 5 uniform misfit intervals (4 models per interval, 20 models in total) which are shown in Figs. 13 and 14, i.e. these are not the best 20 models (for the given parametrization).

7.2   Travel-time average velocities and ground type

The distribution of the travel-time average velocities at different depths was computed for the selected models. $V_{s,30}$ is found to be $374\,\mathrm{m/s}$, which corresponds to ground type B in Eurocode 8 [CEN, 2004], and C for SIA261 [SIA, 2014].

	Mean (m/s)
$V_{s,5}$	203
$V_{s,10}$	258
$V_{s,20}$	332
$V_{s,30}$	374
$V_{s,40}$	405
$V_{s,50}$	432
$V_{s,100}$	529

Table 4: Travel time averages at different depths from the inverted models.

7.3   SH transfer function and quarter-wavelength velocity

The quarter-wavelength velocity approach [Joyner et al., 1981] provides, for a given frequency, the average velocity at a depth corresponding to 1/4 of the wavelength of interest. It is useful to identify the frequency limits of the experimental data (minimum frequency in dispersion curves at $1.5\,\mathrm{Hz}$ and ellipticity peak at $0.8\,\mathrm{Hz}$ here). The results using this proxy show that the dispersion curves constrain the profiles down to $100\,\mathrm{m}$ and the ellipticity down to $200\,\mathrm{m}$ (Fig. 16). Moreover, the quarter wavelength impedance-contrast introduced by Poggi et al.
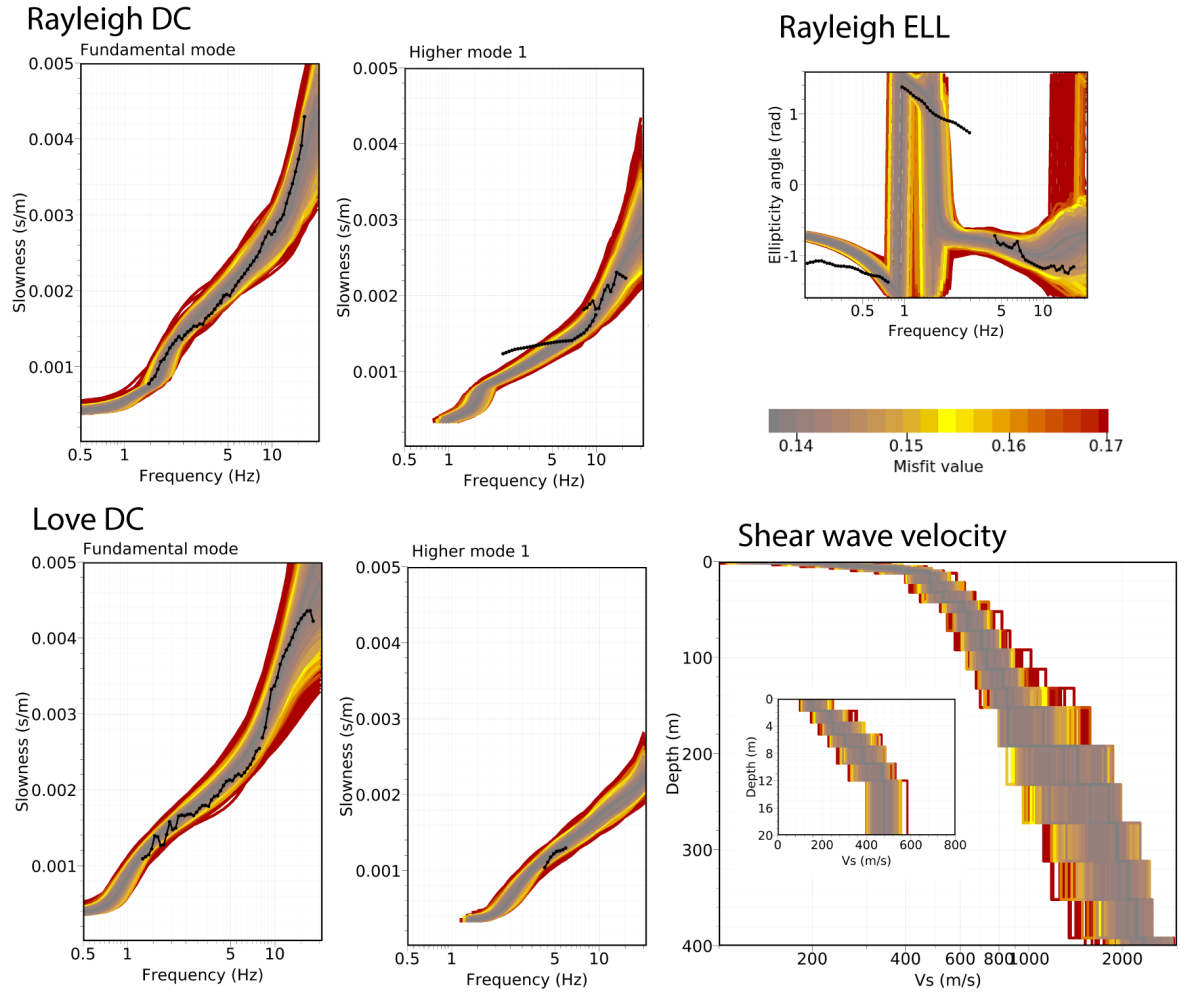
Figure 13: Comparison between the inverted and measured Rayleigh and Love wave dispersion curves for the different modes and the Rayleigh wave ellipticity curves. The corresponding inverted ground profiles in terms of V_s are plotted at the bottom right. Fixed-depth layering was assumed here for all layers.
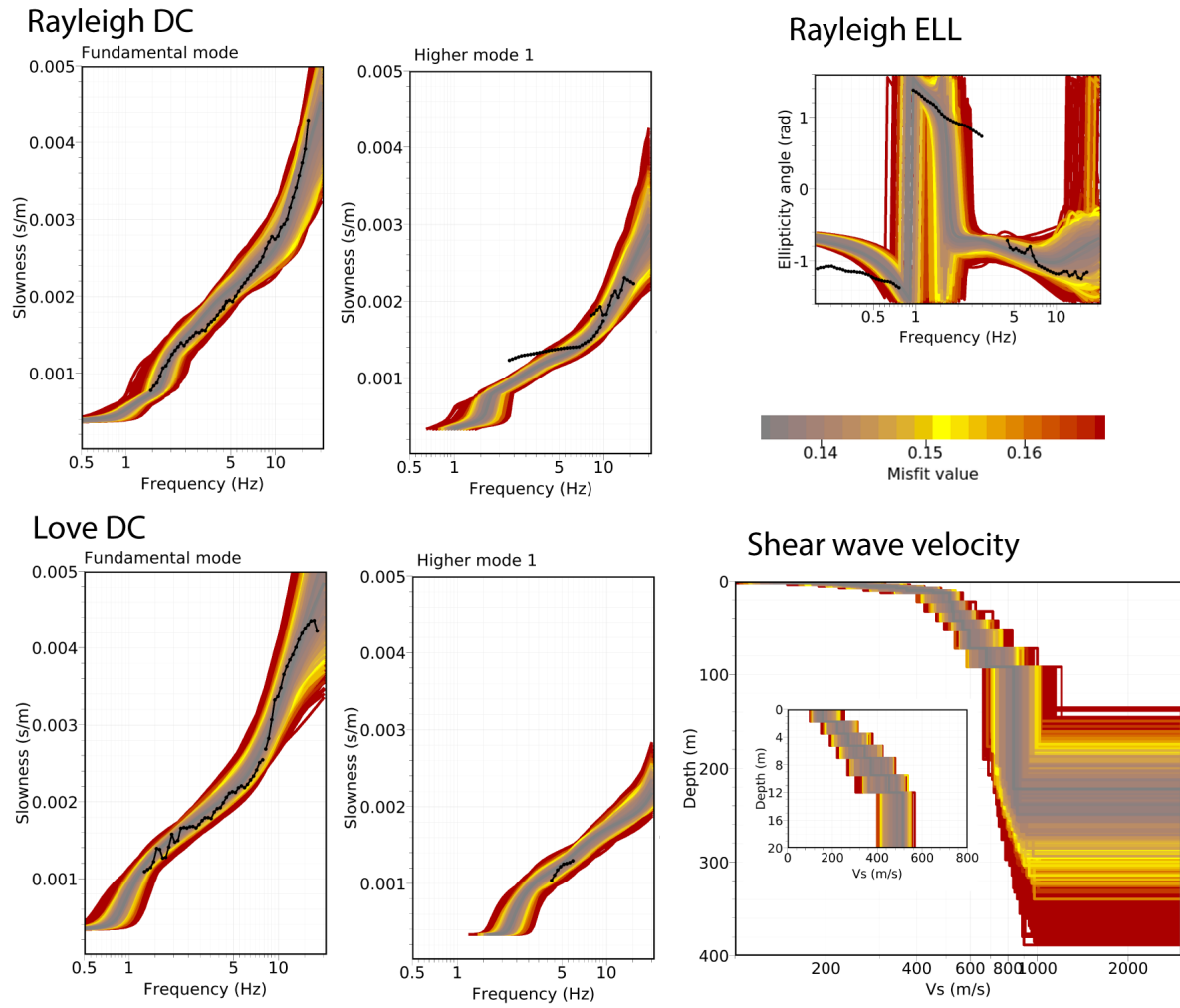
Figure 14: Comparison between the inverted and measured Rayleigh and Love wave dispersion curves for the different modes and the Rayleigh wave ellipticity curves. The corresponding inverted ground profiles in terms of V_s are plotted at the bottom right. Fixed-depth layering was assumed for the top part of the model, while the sediment/bedrock interface was left free.
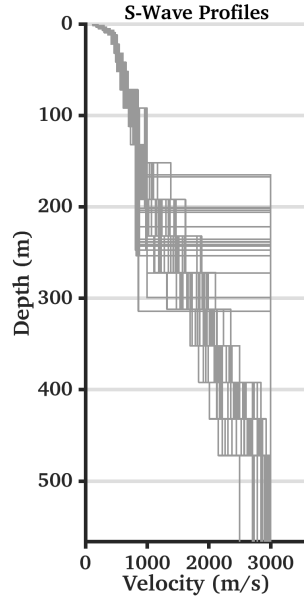
Figure 15: V_s ground profiles for the selected 42 models.

[2012] is also displayed in the figure. It corresponds to the ratio between two quarter-wavelength average velocities, respectively from the top and the bottom part of the velocity profile, at a given frequency [Poggi et al., 2012]. It shows a trough (inverse shows a peak) at the resonance frequency.

Moreover, the theoretical SH-wave transfer function for vertical propagation [Roesset, 1970] is computed from the inverted profiles. It is compared to the empirical amplification measured for earthquake recordings at station SARE (Fig. 17). In this case, the models are predicting an amplification peak of 3 at the fundamental frequency of 0.8 Hz, resonance peak at 2 Hz, and smoother high-frequency amplification (above 4 Hz). Below 3 Hz, the empirical amplification is more smooth than the 1D modeling, probably because the presence of basin effects, such as edge-generated surface waves.

8   Conclusions

The array measurements presented in this study were successful in deriving a velocity model for the site of station SARE. We found a first layer of approximately 12 m characterized by linear increase of shear wave velocities from $200 \, \text{m/s}$ to $500 \, \text{m/s}$ corresponding likely to un-consolidated soils or moraine. Below, the velocity is increasing less rapidly from $500 \, \text{m/s}$ to $800 \, \text{m/s}$ down to 200 m. The bedrock depth is not very well resolved, a strong jump of shear wave velocities is not required even by the singularity of the ellipticity angle. Nevertheless, shear wave velocity increases significantly below 200 m. This corresponds likely to the base of the unconsolidated sediments which 170 m according to Swisstopo.

$V_{s,30}$ is $374 \, \text{m/s}$ corresponds to ground type B in Eurocode 8 [CEN, 2004], and C for SIA261 [SIA, 2014]. The theoretical 1D SH transfer function and impedance contrast of the quarter-wavelength velocity computed from the inverted profiles show moderate amplifications. Record-ings of the station confirm the low-frequency amplification, while the high-frequency amplification (above 4 Hz) is slightly higher for the empirical amplification function.
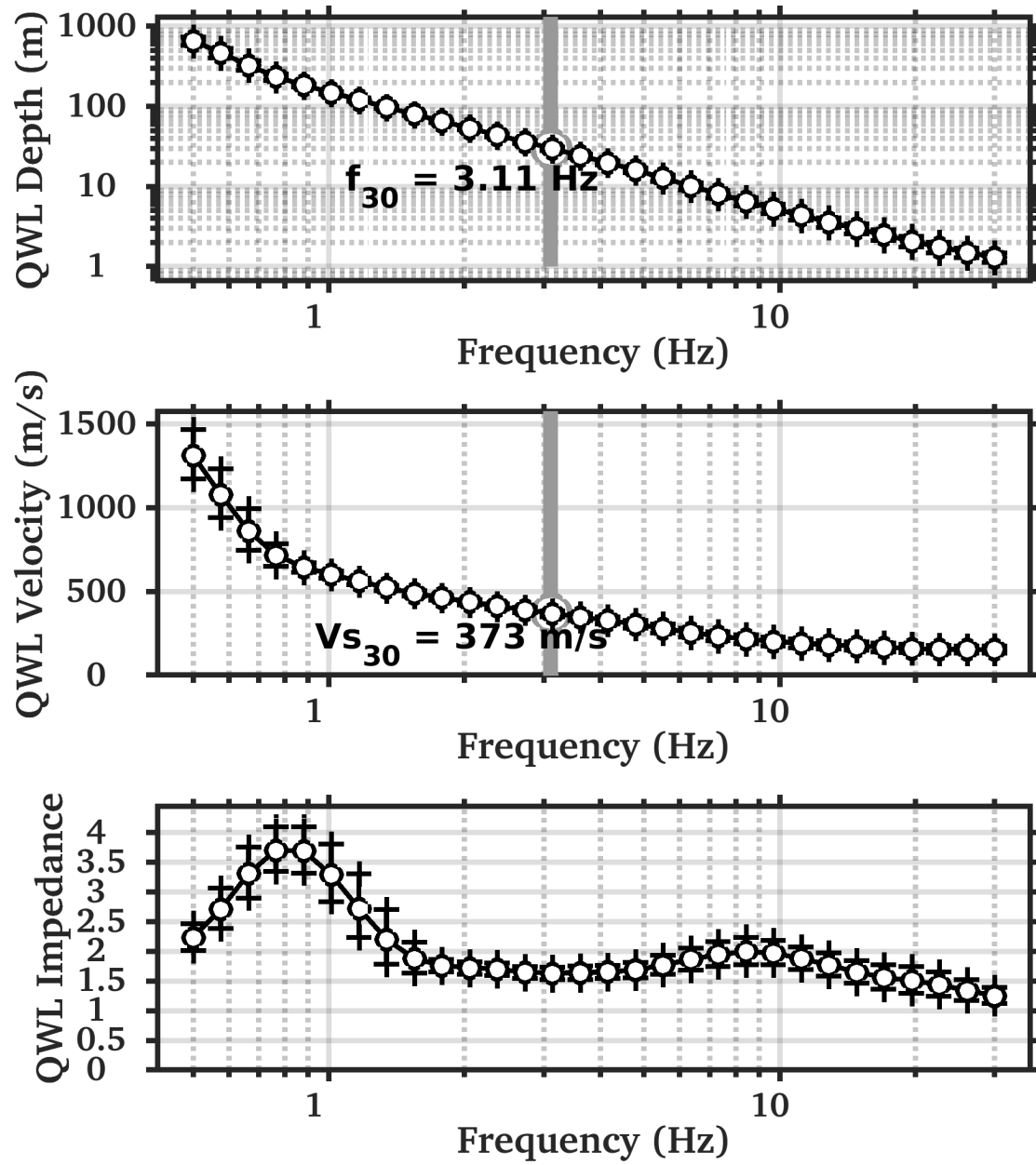
Figure 16: Quarter wavelength velocity representation of the velocity profile (top: depth, centre: velocity, bottom: inverse of the impedance contrast). The grey bar corresponds to $V_{s,30}$.
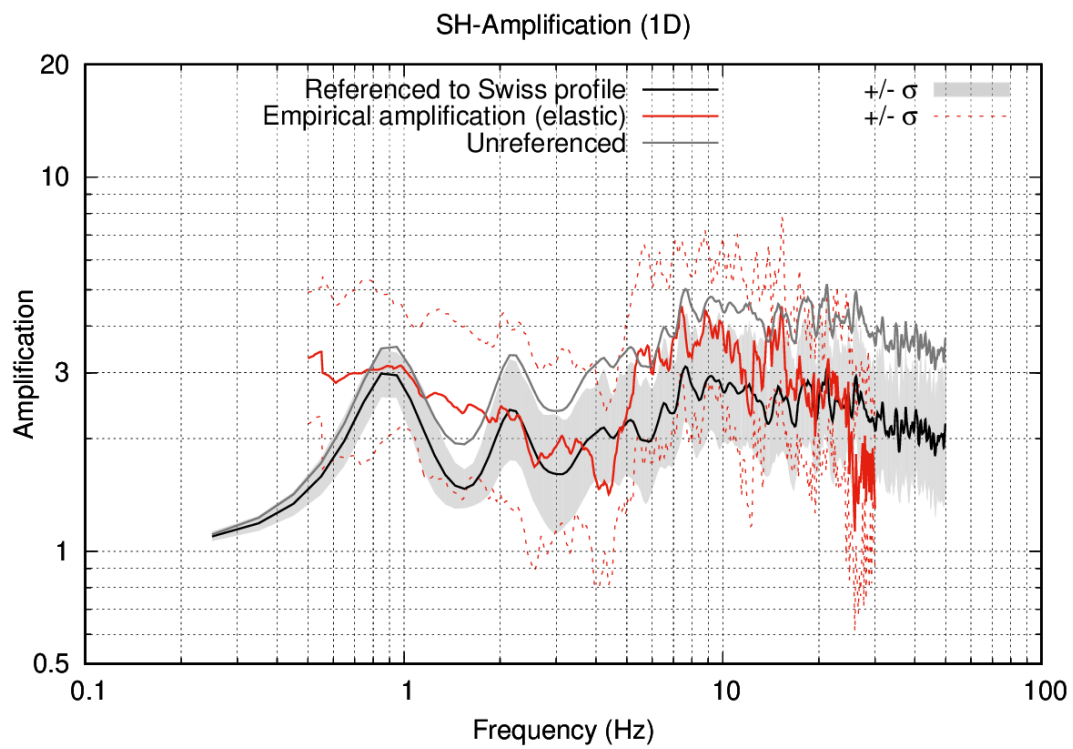
Figure 17: Mean SH transfer function referenced to the profile's bedrock (solid gray) and referenced to the Swiss reference profile (solid black) with standard deviation bounds (gray shade). The elastic empirical amplification function is shown by the red solid curve together with standard deviation bounds (dashed red curves).

Acknowledgements

References

Sylvette Bonnefoy-Claudet, Fabrice Cotton, and Pierre-Yves Bard. The nature of noise wavefield and its applications for site effects studies. *Earth-Science Reviews*, 79(3-4): 205–227, December 2006. ISSN 00128252. doi: 10.1016/j.earscirev.2006.07.004. URL http://linkinghub.elsevier.com/retrieve/pii/S0012825206001012.

Jan Burjánek, Gabriela Gassner-Stamm, Valerio Poggi, Jeffrey R. Moore, and Donat Fäh. Ambient vibration analysis of an unstable mountain slope. *Geophysical Journal International*, 180(2):820–828, February 2010. ISSN 0956540X. doi: 10.1111/j.1365-246X.2009.04451.x. URL http://gji.oxfordjournals.org/cgi/doi/10.1111/j.1365-246X.2009.04451.xhttp://doi.wiley.com/10.1111/j.1365-246X.2009.04451.x.

CEN. *Eurocode 8: Design of structures for earthquake resistance - Part 1: General rules, seismic actions and rules for buildings*. European Committee for Standardization, en 1998-1: edition, 2004.

Donat Fäh, Fortunat Kind, and Domenico Giardini. A theoretical investigation of average H/V ratios. *Geophysical Journal International*, 145(2):535–549, May 2001. ISSN 0956540X. doi: 10.1046/j.0956-540x.2001.01406.x. URL http://doi.wiley.com/10.1046/j.0956-540x.2001.01406.x.

Donat Fäh, Gabriela Stamm, and Hans-Balder Havenith. Analysis of three-component ambient vibration array measurements. *Geophysical Journal International*, 172(1):199–213, January 2008. ISSN 0956540X. doi: 10.1111/j.1365-246X.2007.03625.x. URL http://doi.wiley.com/10.1111/j.1365-246X.2007.03625.xhttp://gji.oxfordjournals.org/cgi/doi/10.1111/j.1365-246X.2007.03625.x.

Donat Fäh, Marc Wathelet, Miriam Kristekova, Hans-Balder Havenith, Brigitte Endrun, Gabriela Stamm, Valerio Poggi, Jan Burjánek, and Cécile Cornou. Using Ellipticity Information for Site Characterisation. Technical report, NERIES JRA4 Task B2, 2009.

William B. Joyner, Richard E. Warrick, and Thomas E. Fumal. The effect of Quaternary alluvium on strong ground motion in the Coyote Lake, California, earthquake of 1979. *Bulletin of the Seismological Society of America*, 71(4):1333–1349, 1981.

Stefano Maranò, C. Reller, H.-A. Loeliger, and Donat Fäh. Seismic waves estimation and wave field decomposition: Application to ambient vibrations. *Geophysical Journal International*, 191:175–188, 2012.

Valerio Poggi and Donat Fäh. Estimating Rayleigh wave particle motion from three-component array analysis of ambient vibrations. *Geophysical Journal International*, 180(1):251–267, January 2010. ISSN 0956540X. doi: 10.1111/j.1365-246X.2009.04402.x. URL http://doi.wiley.com/10.1111/j.1365-246X.2009.04402.x.

Valerio Poggi, Benjamin Edwards, and Donat Fäh. Characterizing the Vertical-to-Horizontal Ratio of Ground Motion at Soft-Sediment Sites. *Bulletin of the Seismological Society of America*, 102(6):2741–2756, December 2012. ISSN 0037-1106. doi: 10.1785/0120120039. URL http://www.bssaonline.org/cgi/doi/10.1785/0120120039.

G.A. Prieto, R.L. Parker, and F.L. Vernon III. A fortran 90 library for multitaper spectrum analysis. *Computers & Geosciences*, 35(8):1701 – 1710, 2009. ISSN 0098-3004. doi: http://dx.doi.org/10.1016/j.cageo.2008.06.007. URL http://www.sciencedirect.com/science/article/pii/S0098300409000077.

J.M. Roesset. Fundamentals of soil amplification. In R. J. Hansen, editor, *Seismic Design for Nuclear Power Plants*, pages 183–244. M.I.T. Press, Cambridge, Mass., 1970. ISBN 978-0-262-08041-5. URL http://mitpress.mit.edu/catalog/item/default.asp?ttype=2&tid=5998.

SIA. *SIA 261 Einwirkungen auf Tragwerke*. Schweizerischen Ingenieur- und Architektenverein, Zürich, sia 261:2014 edition, 2014.

Marc Wathelet. An improved neighborhood algorithm: Parameter conditions and dynamic scaling. *Geophysical Research Letters*, 35(9):1–5, May 2008. ISSN 0094-8276. doi: 10.1029/2008GL033256. URL http://www.agu.org/pubs/crossref/2008/2008GL033256.shtml.

Marc Wathelet, Denis Jongmans, Matthias Ohrnberger, and Sylvette Bonnefoy-Claudet. Array performances for ambient vibrations on a shallow structure and consequences over Vs inversion. *Journal of Seismology*, 12(1):1–19, October 2008. ISSN 1383-4649. doi: 10.1007/s10950-007-9067-x. URL http://link.springer.com/10.1007/s10950-007-9067-x.